RAA 2014 Vol. **14** No. **2**, 207–220 doi: 10.1088/1674–4527/14/2/008
http://www.raa-journal.org *http://www.iop.org/journals/raa*

Research in Astronomy and Astrophysics

On the line profile changes observed during the X2.2 class flare in the active region NOAA 11158

Ankala Raja Bayanna[1], Brajesh Kumar[1], Parameswaran Venkatakrishnan[1], Shibu Kunchandy Mathew[1], Belur Ravindra[2], Savita Mathur[3] and Rafael A Garcia[4]

[1] Udaipur Solar Observatory, Physical Research Laboratory, Dewali, Badi Road, Udaipur 313 004, India; *bayanna@prl.res.in*
[2] Indian Institute of Astrophysics, II Block, Koramangla, Bangalore 560034, India
[3] Space Science Institute, 4750 Walnut Street Suite#205, Boulder, CO 80301, USA
[4] Laboratoire AIM, CEA/DSM-CNRS, Université Paris 7 Diderot, IRFU/SAp, Centre de Saclay, 91191, Gif-sur-Yvette, France

Received 2013 July 17; accepted 2013 October 11

Abstract The solar active region NOAA 11158 produced a series of flares during its passage through the solar disk. The first major flare (of class X2.2) of the current solar cycle occurred in this active region on 2011 February 15 around 01:50 UT. We have analyzed the Dopplergrams and magnetograms obtained by the Helioseismic and Magnetic Imager (HMI) instrument onboard *Solar Dynamics Observatory* to examine the photospheric velocity and magnetic field changes associated with this flare. The HMI instrument provides high-quality Doppler and magnetic maps of the solar disk with $0.5''$ spatial scale at a cadence of 45 s along with imaging spectroscopy. We have identified five locations of velocity transients in the active region during the flare. These transient velocity signals are located in and around the flare ribbons as observed by *Hinode* in the Ca II H wavelength and the footpoints of hard X-ray enhancement are in the energy range 12–25 keV from *RHESSI*. The changes in shape and width of two circular polarization states have been observed at the time of transients in three out of five locations. Forward modeling of the line profiles shows that the change in atmospheric parameters such as magnetic field strength, Doppler velocity and source function could explain the observed changes in the line profiles with respect to the pre-flare condition.

Key words: Sun: activity — Sun: sunspot — Sun: flares — Sun: spectroscopy — Sun: velocity and magnetic fields

1 INTRODUCTION

In solar flares, the magnetic energy stored in the active regions is catastrophically released in the form of a large amount of thermal energy and energetic particles moving with relativistic speeds. Investigations have been made to study the changes related to the flare in various magnetic properties associated with the active regions. Significant changes are known to take place in magnetic shear (Hagyard et al. 1999; Tiwari et al. 2010), magnetic flux (Sudol & Harvey 2005; Wang et al. 2009;

Wang et al. 2011; Wang et al. 2012), magnetic helicity (Moon et al. 2002; Ravindra et al. 2011) and magnetic energy (Metcalf et al. 2005; Ravindra & Howard 2010; Sun et al. 2012) during the flares.

Apart from these observed changes in properties of the magnetic field during the flare, it is also believed that the solar flares can excite oscillations in the Sun. Wolff (1972) suggested that large solar flares would cause a thermal expansion that would launch a wave of compression to move sub-sonically into the solar interior, thereby stimulating solar oscillations. Following this, several researchers have made an attempt to study the effect of flares on the acoustic velocity oscillations of the Sun discovered in the 1960s (Leighton et al. 1962). These global *p*-mode oscillations are excited by turbulence in the convective layers of the Sun (Leibacher & Stein 1971, Goldreich et al. 1994). Haber et al. (1988) reported an increase in the average power of intermediate degree modes after a flare. The first detection of 'solar quakes' inside the Sun was reported by Kosovichev & Zharkova (1998) during the X2.6 class flare on 1996 July 9. Since then, there have been several reports on the local and global effects of a flare on the solar velocity oscillations (Kumar et al. 2010; Kumar et al. 2011, and references therein).

In this paper, we present a detailed study of changes in velocity and magnetic fields associated with the flare observed in the active region NOAA 11158 during the X2.2 class flare on 2011 February 15. Full-disk Dopplergrams and magnetograms obtained by the Helioseismic and Magnetic Imager (HMI; Schou et al. 2012) onboard the *Solar Dynamics Observatory* (*SDO*; Pesnell et al. 2012) spacecraft were used to study these changes in the active region. The active region NOAA 11158 was located close to the disk center (S21, W21). The active region was comprised of four sunspots, with the central one having a δ-type magnetic configuration which produced an X2.2 class flare on 2011 February 15. The active region also produced a few M-class flares in the subsequent days in addition to a few weaker flares prior to this flare event. As seen in soft X-ray flux (1–8 Å) data from the Geostationary Operational Environmental Satellite (*GOES*), the flare started at 01:44 UT, peaked at 01:56 UT and ended at 02:06 UT. Wang et al. (2012) showed that strong magnetic shear developed in this active region caused by the rapid evolution of the horizontal magnetic field and it played an important role for triggering this X-class flare. Vemareddy et al. (2012) and Song et al. (2013) have studied the magnetic non-potentiality parameters of this active region and concluded that rotational motion of the sunspot played a significant role in increasing the non-potentiality, thereby leading to the observed multiple flares and CME event in this active region.

Using *SDO*/HMI data, Martinez et al. (2011) carried out line profile analysis of a white-light M-class flare for which they observed a step-wise change in the line-of-sight (LOS) magnetic field at the flare footpoints. They concluded that although the line remains in the absorption, there was a shift in the line profile towards blue in the footpoints of the flaring region. However, they did not observe any changes in the line width and shape. In this event of the X2.2-class flare, we have found five different locations in the active region which show enhanced velocity signals during the flare. These locations also show significant changes in magnetic signals during the flare. Contrary to the observations of Martinez et al. (2011) for the M-class flare, here we observe that three out of the five locations show line profile changes. We use forward modeling of the pre-flare profiles of the two circular polarization states (*LCP* and *RCP*) to show that the observed changes in the line profiles during the flare can indeed be principally interpreted as due to magnetic and velocity changes.

2 THE OBSERVATIONAL DATA

In this work, we use photospheric observations of the active region NOAA 11158 centered at 6173 Å. The data consist of full-disk images of intensity, magnetic field and velocity at a cadence of 45 s for the period starting from 01:00 UT to 02:30 UT obtained from the HMI instrument onboard *SDO*. We have also used *LCP* and *RCP* data from HMI for examining the line profile changes during the flare. HMI observes both these polarizations at six wavelength positions along the line profile, sequentially, at an approximate cadence of 3.75 s, giving an overall cadence of 45 s.

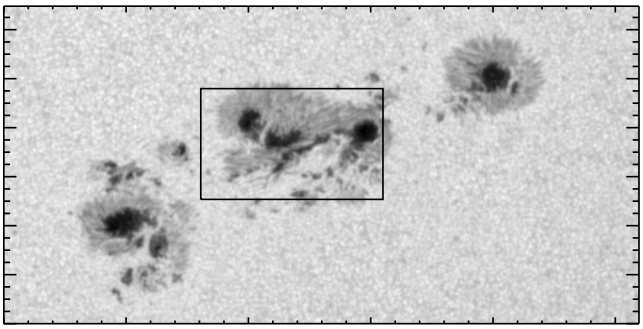

Fig. 1 The continuum image of the active region NOAA 11158 as observed with *SDO*/HMI. The box shown in thick lines contains the region which produced the X2.2 class flare. The total field-of-view is 260×130 arcsec^2.

From the Solar Optical Telescope (SOT; Tsuneta et al. 2008) onboard *Hinode* (Kosugi et al. 2007), we have obtained filtergrams of Ca II H centered at 3968 Å, recorded at a cadence of 5 min starting from 01:00 to 02:30 UT. However, the observing cadence of the instrument during the period from 01:50 to 02:02 UT was set as 20 s to have a better observation of the temporal evolution of the flare. The spatial scale of these Ca II H images is $\sim 0.1''$ per pixel. These filtergrams reveal that the flare is a typical two-ribbon type and the ribbons lie on both sides of the polarity inversion line. These observations are used to identify the location of flare kernels.

We have also used the hard X-ray (HXR) spectral data from the *Reuven Ramaty High Energy Solar Spectroscopic Imager (RHESSI;* Lin et al. 2002*)* in the energy band 12–25 keV to compare the temporal evolution of the HXR peak with the spatial coincidence of the velocity and magnetic field changes during the flare.

3 DATA ANALYSIS

A grid of area 260×130 arcsec^2 containing the active region NOAA 11158 (c.f. Fig. 1) is extracted from the full-disk intensity image of HMI. The rasters of these intensity images were co-aligned using a two-dimensional cross-correlation technique to a sub-pixel accuracy. Later on, the co-aligned rasters of these intensity images were used to co-align the co-temporal Dopplergrams, magnetograms and images representing the circular polarizations from HMI. The Ca II H filtergrams obtained from *Hinode*/SOT were also co-aligned with respect to intensity images obtained from HMI by reducing the pixel resolution from $0.1''$ to $0.5''$.

The *RHESSI* images are reconstructed using the CLEAN algorithm (Hurford et al. 2002) for $1.0''$ per pixel spatial scale and further interpolated to $0.5''$ per pixel to match the HMI image scale. The field of view of the reconstructed images is $128'' \times 128''$. These images are co-aligned with the HMI data sets using the header information available in both the data. However, because of the low-resolution of the *RHESSI* images, the accuracy of the co-alignment of *RHESSI* images with respect to the images obtained by HMI is about $1.0''$.

3.1 Identification of Localized Velocity Transients

A two-point backwards difference filter (García & Ballot 2008) is applied to the time series of images to remove the slowly varying solar background features. Thus, we obtain a series of difference images for the Dopplergrams. Using this sequence of difference images, we construct a 'depth image' by obtaining the difference between the minimum and maximum values of the time series for each

pixel. From this, we identified the pixels with velocity values larger than 1 km s^{-1} as the locations of large velocity flows during the flare.

We have also constructed two root-mean-square (rms) maps. One is from a sequence of Dopplergrams obtained before the flare starting from 01:10 to 01:40 UT. Another one is from Dopplergrams obtained during the flare event starting from 01:40 to 02:10 UT. A difference image was constructed from these two rms images. The pixels with enhanced velocity in the active region were identified by using a threshold velocity of $\pm$ 200 m s^{-1} in the aforesaid difference of rms images from the Dopplergrams. The threshold of $\pm$200 m s^{-1} is equivalent to $\pm 3\sigma$ of a quiet Sun.

Using the above criteria, we selected a set of pixels showing enhanced velocity signals. All of these are located in the central sunspot of the active region, which produced the X2.2 class flare on 2011 February 15. We grouped all these pixels into five regions (or kernels), namely, K_1, K_2, K_3, K_4 and K_5 as shown in Figure 2. Here, the kernel K_5 contains the weakest velocity transient relative to K_1, K_2, K_3 and K_4. For comparison, we considered a quiet region of size 3×3 pixels away from the active region. The regions of velocity transients K_1 and K_2 identified by us coincide with the locations of seismic sources shown by Kosovichev (2011); K_4 coincides with the seismic source shown by Zharkov et al. (2013). In addition to this, the location K_2 coincides with the transient velocity location shown by Maurya et al. (2012) as well.

As indicated earlier, a raster of the active region along with the locations of kernels with transient velocity signals is shown in Figure 2. The *RHESSI* HXR contours corresponding to 95%, 75%, 50% and 25% of the maximum value of the temporally averaged image during the period 01:50–02:00 UT are overlaid on the intensity image. The time period 01:50–02:00 UT is considered for constructing the average image as this duration spans the impulsive phase of the flare as seen in the HXR light curve from *RHESSI*. The velocity and magnetic changes are also observed during this period. Here, we report that the kernels K_2, K_3, K_4 and K_5 spatially coincide with the location of HXR enhancement. It is important to note that all these kernels are located in the areas with weaker HXR emission, but the kernel K_1 is slightly displaced from the location of enhancement in HXR. In this regard, it can be noted that Kosovichev (2011) has already pointed out that the kernel K_1 (or Impact 1) appears before the impulsive phase of the HXR emission.

We also overlaid the contours of the flare ribbons seen in the Ca II H image constructed as a temporal average over the duration 01:50–02:00 UT on the intensity image of the active region as observed by *SDO*/HMI. All the kernels, K_1, K_2, K_3, K_4 and K_5, are located in and around the flare-ribbons, as is evident from Figure 2. However, it is interesting to note that these transient signals are not located in the central part of the flare ribbons.

In order to examine the behavior of the velocity signals within the flare ribbons with respect to a non-flaring magnetic region, we plot a histogram (c.f., Fig. 3) of rms Doppler velocity (DV) of all the pixels contained in the flare ribbons for the epochs before, during and after the flare. We observe that the rms value of the DV for the aforementioned pixels is higher during the flare in comparison to that before and after the flare. A similar analysis is done for another sunspot group (rightmost in Fig. 1) in the same active region and also in a quiet region. Both show no change in the histograms during the flare compared to before and after the flare.

3.2 Temporal Variations of Velocity and Magnetic Fields in the Identified Locations of Velocity Transients

In Figure 4, we show the time series of DV and magnetic field ($B_{\rm LOS}$) variations over five locations (K_1, K_2, K_3, K_4 and K_5) and one of the quiet Sun locations. As evident from Figure 4, almost all the regions show a sudden jump in the DV as well as in the $B_{\rm LOS}$ during the flare, except K_3, where we observe a gradual decrease in the $B_{\rm LOS}$ from 450 G to 120 G. In general, DV returns back to the pre-flare levels after the flare but a permanent change of approximately 100 G is observed in the case

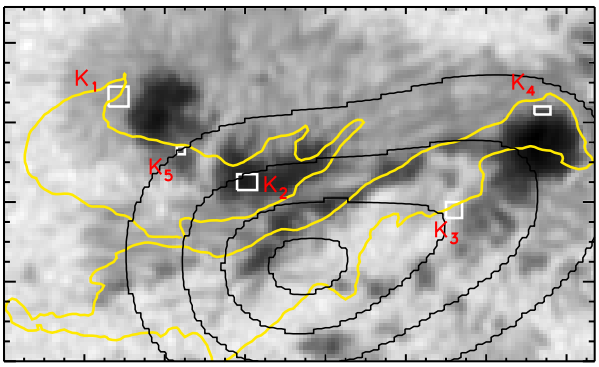

Fig. 2 The continuum image showing part of the active region NOAA 11158, which is used in our analysis. K_1, K_2, K_3, K_4 and K_5 represent the kernels of the significantly enhanced velocity signals. The yellow contours show the location of flare ribbons extracted from the temporally averaged Ca II H images spanning the period 01:50–02:00 UT. The total field-of-view is $\sim 75\times45$ arcsec^2. Contours of the temporally averaged HXR image from *RHESSI* spanning the period 01:50–02:00 UT are shown as black solid lines. Starting from the center, the four contour levels correspond to 95%, 75%, 50% and 25% of the maximum value, respectively.

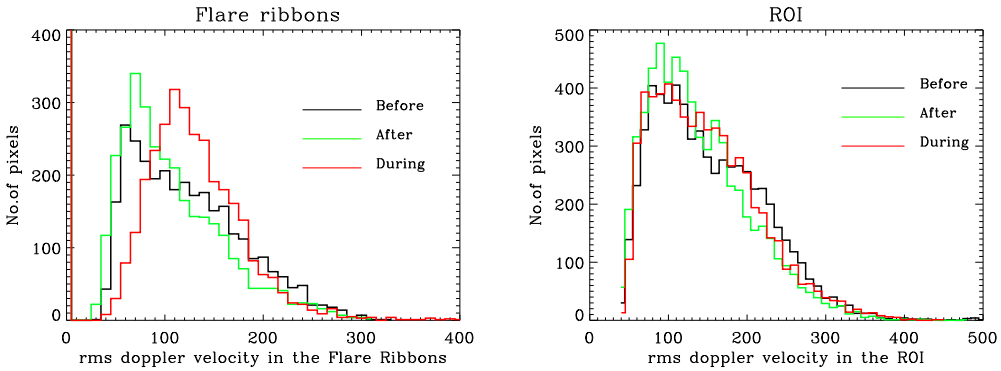

Fig. 3 *Left*: Histogram of rms DV of all the pixels contained in the flare ribbons for the epochs before (*black*), during (*red*) and after (*green*) the flare. *Right*: Histogram of rms DV for the non-flaring sunspot group (rightmost in Fig. 1) in the same active region for the epochs before (*black*), during (*red*) and after (*green*) the flare.

of $B_{\rm LOS}$. Such behaviors of step-function-like changes (or rapid changes) and gradual changes in magnetic fields during M-class and X-class flares have been reported earlier by several researchers (Kosovichev & Zharkova 1999; Kosovichev & Zharkova 2001; Sudol & Harvey 2005; Wang 2007; Wang et al. 2009; Zhao et al. 2009; Wang et al. 2011). In our analysis, it is also observed that in all the cases velocity transients occur prior to the magnetic transients (c.f., Table 1) and the times of velocity and magnetic transients are separated by at least 45 s.

In order to examine the evolution of the HXR light curve during the flare corresponding to the localized positions K_1, K_2, K_3, K_4 and K_5, we have over-plotted the *RHESSI* spectral data (blue-dotted curves) in the energy range 12–25 keV in Figure 4. It is observed that the HXR energy

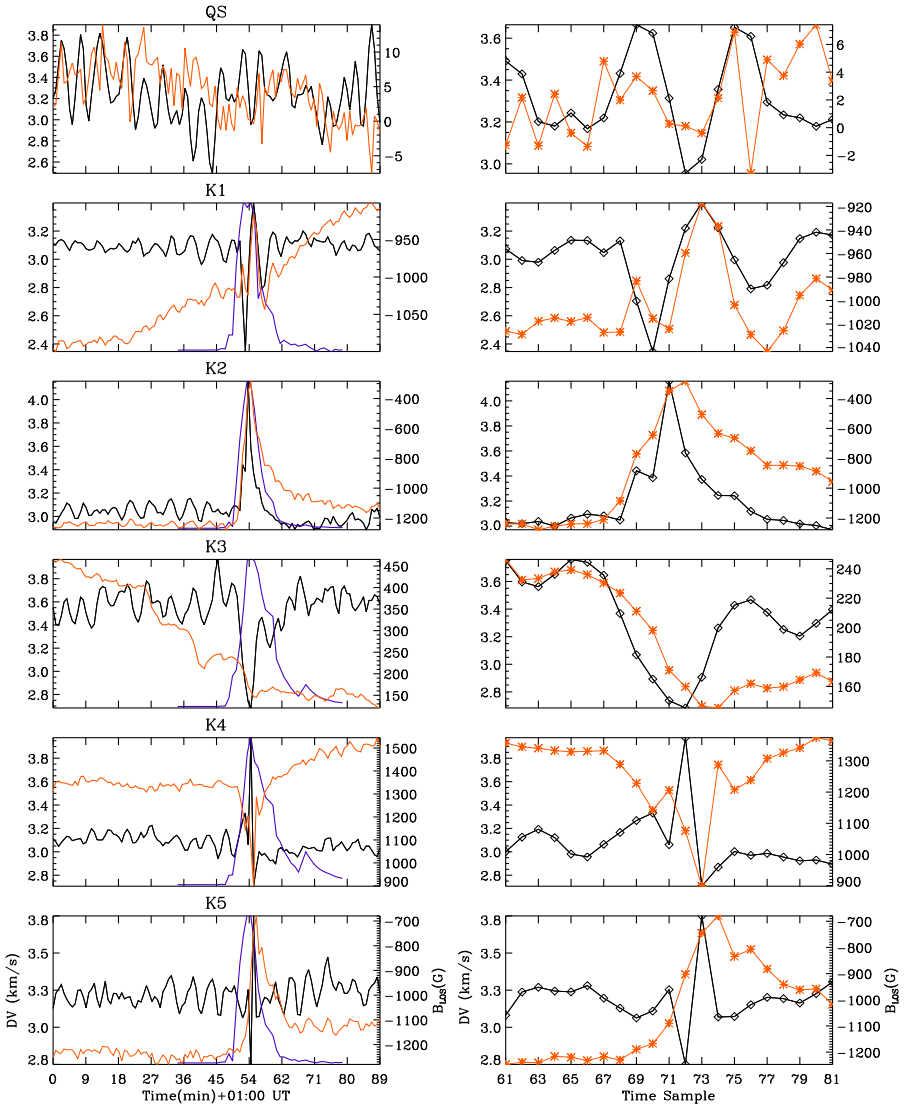

Fig. 4 *Left*: Temporal evolution of DV and $B_{\rm LOS}$ (over-plotted orange color) for the duration 01:00–02:30 UT. *Right*: the same data for the period 01:45–02:00 UT of the kernels K_1, K_2, K_3, K_4 and K_5. The over-plotted blue curve shows the temporal evolution of HXR flux from *RHESSI* in the energy band 12–25 keV corresponding to the localized positions. The panels in the top show the DV and $B_{\rm LOS}$ for a quiet area away from the active region.

peaks either at 01:53 UT or 01:54 UT in all these locations. For the kernels K_2, K_3, K_4 and K_5, we observe that the peaks of velocity transients are seen within a minute from the peak time of HXR evolution at these locations in the energy band 12–25 keV. This result is compatible with the theoretical simulations of Zharkova & Zharkov (2007). However, the peak time of velocity transients observed at the kernel K_1 appears during the peak time of the HXR variations. It can be noted that the HXR light-curve in the energy band 12–25 keV at the kernel K_1 has a structured peak. Hence, it is difficult to conclude in this case whether the HXR impulse precedes the velocity transients.

Table 1 Time (UT) of Velocity and Magnetic Transients in the Identified Kernels

Kernel	Velocity	Magnetic field (LOS)
K_1	01:52:24	01:54:39
K_2	01:53:09	01:53:54
K_3	01:53:54	01:55:24
K_4	01:53:54	01:54:39
K_5	01:53:54	01:55:24

3.3 Line Profile Changes Associated with the Identified Locations of Velocity and Magnetic Transients

It is understandable that the large velocity and strong magnetic field can cause the line profile of Fe I to be out of the working range of the *SDO*/HMI inversion algorithm, which is used for deriving the LOS velocity and magnetic field measurements. In this regard, the limitation of the HMI observables algorithm depends on the surface velocity, magnetic field strength, orbital velocity of the spacecraft and the location of the region of interest on the solar disk. As the total wavelength range covered by HMI is only about 344 mÅ, the Fe I line moves out of the working range of the HMI algorithm for DVs larger than $\pm$8.3 km s^{-1} or an equivalent magnetic field strength of 3800 G, which yields a bad result (Couvidat et al. 2012). In all the kernels identified by us, the maximum velocity, including the orbital velocity of the spacecraft, is 4.2 km s^{-1} and the maximum field strength is less than 1500 G. Thus, the observed LOS velocity and magnetic field strength are within the working range of the instrument.

On the other hand, in the absence of spectro-polarimetric observations, it has always been a concern that large velocity flows or rapid changes in magnetic fields observed during the flares could be the result of artifacts arising due to distortions in the line profiles (Ding et al. 2002; Qiu & Gary 2003, and references therein). Wang et al. (2011), for the first time, analyzed spectral line profiles of a flaring region which showed abrupt changes in magnetic flux during three successive M-class solar flares in the active regions NOAA 10039 and NOAA 10044 observed on 2002 July 6. They used data observed by the Imaging Vector Magnetograph (IVM) at Mees solar observatory to check possible line profile changes during the flares. They observed that the fluctuations in the width, depth and central wavelength of the lines were less than 5% and also they ruled out any obvious signature of changes in line profile associated with the flare. Similarly, Martinez et al. (2011) did not find any change in the line width and shape during a white-light M-class flare using the spectro-polarimetric data from *SDO*/HMI. Zhao et al. (2009) attempted to quantify the flare-induced signals during an X2.6 class flare observed on 2005 January 15, and studied the correlation of the flare-induced signal with real magnetic changes during the flare. They used vector magnetic field data from Big Bear Solar Observatory along with co-temporal Ca I 6103 Å and H_α observations for their study. They found that the flare-induced signal appeared in the form of apparent polarity reversal in the observed magnetograms. Their analysis also revealed that the flare-induced signal appeared both in circular polarization measurements and transverse magnetograms.

Here, we analyze the spectro-polarimetric profiles for this X2.2 class flare obtained from *SDO*/HMI corresponding to the times of the velocity and magnetic transients at the identified locations. HMI sequentially observes the *LCP* and *RCP* at six wavelength positions in the wavelength range 6173 Å $\pm$ 172 mÅ, at a cadence of 45 s. These polarization data were reproduced by the HMI team by interpolating the raw data to a target time as required.

In order to understand changes associated with the flare in the line profiles of the identified kernels, we examined co-temporal *LCP* and *RCP* profiles for this flare similar to Martinez et al. (2011) for an M-class flare. We used a Gaussian fit with four parameters (continuum intensity (I_c), line depth (I_d), line center wavelength (λ_0), and FWHM (σ); c.f. equation (3) of Couvidat et al. 2012)

for fitting the six measurements ($I_i,\ i = 0, 5$) of *LCP* and *RCP*. Initial values of $I_{\rm d}$ and σ are obtained from Fourier coefficients (c.f. equations (6) and (7) of Couvidat et al. 2012). The initial value of $I_{\rm c}$ is obtained from the maximum of the I_i's, and the wavelength position where the minimum of the I_i's occur is chosen as the initial value of λ_0. This results in an optimum Gaussian fit to the observed *LCP* and *RCP* measurements with a minimized chi-square value.

Based on the above procedure to fit the six measurements, we now examine changes in the line profile in all the kernels.

Figure 5 shows the *LCP* (asterisks) and *RCP* (diamonds) profiles along with their respective spectral fits (blue and red curves) for the epochs: before (column I), at the time of velocity (column II) and magnetic (column III) transients and after the flare (column IV).

In Table 2, we report the line depth, full-width at half maximum, line center of the profiles and chi-square value of the fits for all the epochs.

From Figure 5, it is evident that there are no significant changes in the shape and width of the line profiles at the time of transients for the kernels K_1 and K_3. The kernels K_2, K_4 and K_5 show a change in shape (depth and width) of line profile as well as a local increase in intensity at -34 mÅ and $+172$ mÅ. These wavelength positions are on the wings of the line profile (near the inflection points of the line profiles).

In what follows, we demonstrate, using forward modeling, that these changes in the line profiles of *LCP* and *RCP* in the kernels (K_2, K_4 and K_5) during the transients can be explained in terms of a combined change in DV, B_0 and line depth.

As we are only interested in synthesis of the line profiles for a given change in different atmospheric parameters, we consider the inversion code "MELANIE" which is based on the Milne-Eddington (Skumanich & Lites 1987) model. Using this code, the atmospheric parameters (magnetic

Table 2 Parameters of *LCP* and *RCP* of the Kernels at the Time of Velocity and Magnetic Transients

Kernel	Flare Time	Line Center (mÅ)		Line Width (mÅ)		$\chi^2 \times 10^{-4}$	
		LCP	*RCP*	*LCP*	*RCP*	*LCP*	*RCP*
K_1	Before	14.6	128.1	191.8	239.1	1.36	0.18
	Vel. Transient	0.8	099.7	186.6	213.3	1.40	0.10
	Mag. Transient	25.8	131.6	191.8	244.2	0.32	0.08
	After	20.6	114.4	191.8	211.6	1.04	0.16
K_2	Before	4.3	141.0	225.3	233.9	0.28	0.11
	Vel. Transient	84.3	102.3	104.9	170.3	0.08	0.01
	Mag. Transient	68.8	86.9	124.7	166.8	0.08	0.01
	After	11.2	121.3	255.4	220.2	0.07	0.04
K_3	Before	86.0	63.6	180.6	175.4	0.30	0.40
	Vel. Transient	61.0	47.3	200.4	183.2	0.32	0.42
	Mag. Transient	70.5	60.2	182.3	168.6	0.35	0.53
	After	80.8	68.8	164.2	163.4	0.55	0.62
K_4	Before	157.4	0.86	242.5	192.6	0.08	0.55
	Vel. Transient	126.4	50.7	149.6	142.7	0.19	0.11
	Mag. Transient	99.8	7.7	206.4	216.7	0.05	0.08
	After	172.0	-5.2	251.1	177.2	0.060	0.53
K_5	Before	8.6	139.3	196.9	215.0	0.34	0.31
	Vel. Transient	16.3	100.6	203.8	187.5	0.15	0.02
	Mag. Transient	26.7	87.7	211.6	180.6	0.18	0.020
	After	18.9	135.9	203.8	211.6	0.36	0.16
QS	Before	54.2	54.2	136.7	135.8	2.21	2.23
	Transient	58.5	58.5	141.9	141.9	1.52	1.50
	After	64.5	64.5	148.8	147.9	1.47	1.50

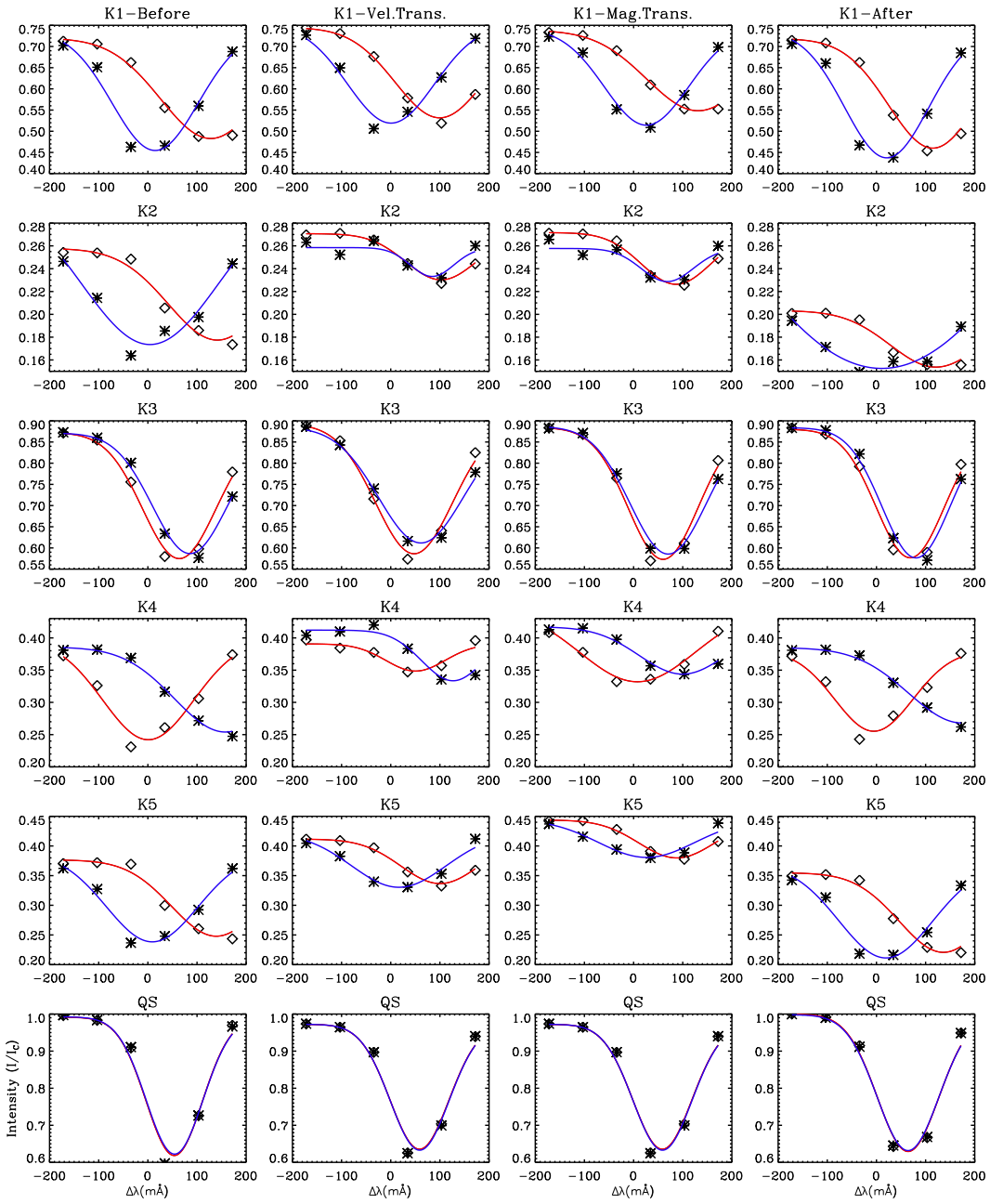

Fig. 5 *LCP* (*blue*) and *RCP* (*red*) profiles of Fe I line for the epochs: pre-flare (*first column*), time of velocity transient (*second column*), time of magnetic transient (*third column*) and post-flare (*fourth column*) for the kernels K_1, K_2, K_3, K_4 and K_5 and quiet Sun (QS), respectively, from top to bottom. The asterisks show the observed spectra for *LCP*, the diamonds show the observed spectra for *RCP*, and the continuous lines show the corresponding spectral fit (*color online*).

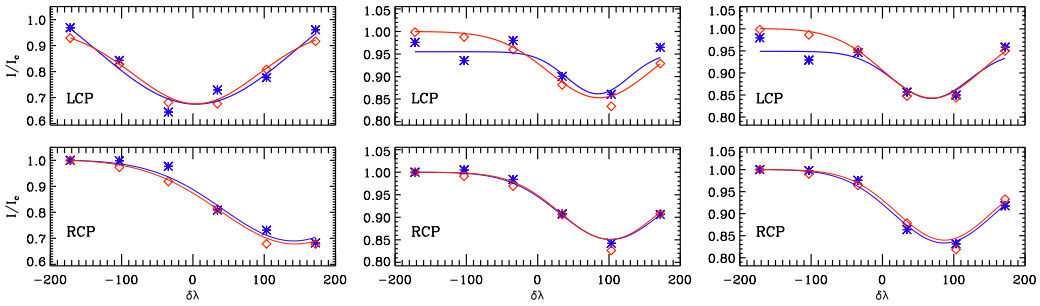

Fig. 6 Comparison of observed (*blue*) and synthesized (*red*) profiles of *LCP* and *RCP* for the kernel K_2 is shown in the top and bottom panels, respectively, at the epochs: before the flare (*left*), at the time of velocity transient (*middle*) and at the time of magnetic transient (*right*). Symbols represent the normalized intensity at different wavelength positions and the continuous line is the corresponding Gaussian fit (*color online*).

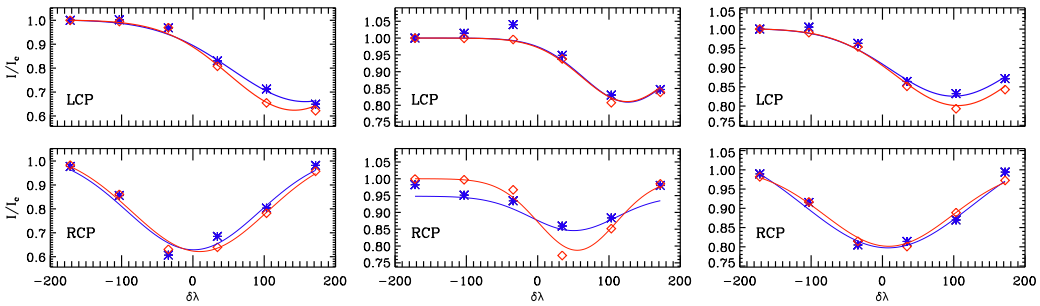

Fig. 7 Same as Fig. 6 but for kernel K_4.

field strength, DV, Doppler width, line strength, damping constant, source function, source gradient and macroturbulence) were adjusted in such a way that simulated profiles of *LCP* and *RCP* derived from modeled Stokes *I* and *V* closely matches the observed profiles of *LCP* and *RCP* at the time of velocity and magnetic transients for each kernel.

In case of K_2, the dominant changes seen are the change in magnetic field strength of about 1400 G and change in velocity of about 1100 m s^{-1} in addition to changes in line strength and source function. For K_4, a change in B_0 of about 1000 G and a change in DV of about 500 m s^{-1} were the dominant changes in the atmospheric parameters in addition to minor changes in line strength, source function and inclination. Similarly, for K_5, the dominant changes seen are the change in B_0 of about 700 G and change in DV of about 500 m s^{-1} in addition to a change in line strength, source function and inclination.

The synthesized line profiles along with observed ones for the kernels K_2, K_4 and K_5 at the time of velocity and magnetic transients are shown in Figures 6, 7 and 8, respectively. In each of these figures, the top row compares observed and synthesized profiles of *LCP* for the epochs: before the flare, at the time of velocity transient and at the time of magnetic transient, respectively, from left to right. Similarly, the bottom row compares observed and synthesized profiles of *RCP*. It is observed that the synthesized profiles are in good agreement with the observed profiles of *LCP* and *RCP*. However, deviations are also seen in the *LCP* profile of K_2 at the time of velocity and magnetic transients and in the *RCP* profile of K_4 at the time of velocity transient.

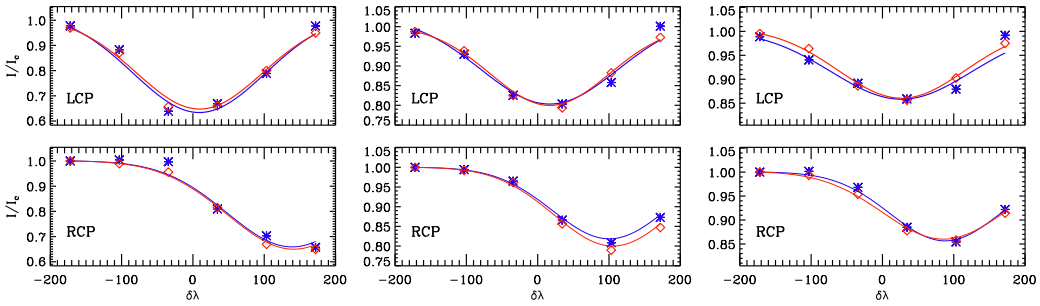

Fig. 8 Same as Fig. 6 but for kernel K_5.

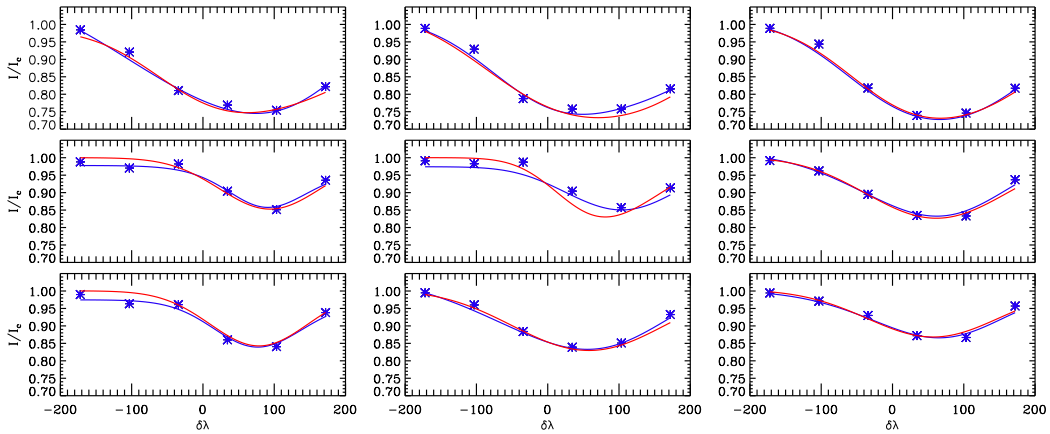

Fig. 9 Comparison of observed (*blue*) and synthesized (*red*) profiles of I (derived from profiles *LCP* and *RCP*) for the kernel K_2, K_4 and K_5 (*left to right*) at the epochs: before the flare (*top*), at the time of velocity transient (*middle*) and at the time of magnetic transient (*bottom*). Symbols represent the normalized intensity at different wavelength positions and the continuous line is the corresponding Gaussian fit.

We reconstructed profiles of Stokes *I* from the profiles of *LCP* and *RCP* to check for any emission or central reversal of the line profile during the transients (c.f., Fig. 9). Here, we do not observe any emission or reversal in the line profiles for these kernels. In summary, forward modeling of the line profiles at the time of transients shows that a significant change in magnetic field strength and DV relative to the pre-flare condition are necessary for achieving the correlation between observed and synthesized profiles for all the kernels.

4 DISCUSSION AND CONCLUSIONS

We have analyzed the response of the solar photospheric velocity flows and associated magnetic fields to the first major flare (of class X2.2) of the current solar cycle that occurred in the active region NOAA 11158 on 2011 February 15. This flare event was well observed by the HMI instrument onboard the *SDO* spacecraft. The HMI instrument provides high-resolution imaging spectroscopy of the active region, including continuum, Doppler and magnetic maps of the solar disk in the photo-

spheric Fe I line centered at 6173 Å. Such features in the HMI data have enabled us to investigate the changes associated with the flare in velocity and magnetic signals observed in the active region NOAA 11158 on 2011 February 15.

In this study, our chief findings are as follows:

(i) The analysis of Dopplergrams of the active region spanning the flare event shows five kernels K_1, K_2, K_3, K_4 and K_5 in the active region which contain enhanced velocity signals that are associated with the flare. These kernels are located in and around the flare ribbons as seen in Ca II H images from SOT/FG onboard *Hinode*. It is also observed that all these kernels, except K_1, are spatially distributed within the HXR brightened location from *RHESSI*. Among these five kernels, some coincide with seismic sources shown by Kosovichev (2011) and Zharkov (2013) and transients shown by Maurya et al. (2012). The kernels show enhanced downflows/upflows with a difference between the minimum and maximum velocities being about 1 km s^{-1}.

(ii) Identified kernels show velocity transients during the impulsive phase of the flare as seen in the *RHESSI* HXR. A comparative study of the temporal evolution of the HXR light curve in the energy band 12–25 keV from *RHESSI* and velocity transients seen in the identified kernels K_1, K_2, K_3, K_4 and K_5 show that, except for K_1, the enhanced velocity signals appear within one minute after the peak time of the HXR in the respective kernels. Thus, it can be assumed that these velocity transients are the photospheric responses of the energetic particles impinging on the solar photosphere during the flare as modeled by Zharkova & Zharkov (2007). However, the structured nature of the peak of the HXR light curve for K_1 makes it difficult to conclude whether the velocity impulse is generated as a result of particle impact. Kosovichev (2011) proposed that for this kernel, the energy transport into the lower atmosphere could have been provided by the saturated heat flux.

(iii) The study of magnetic field variations in the identified locations show that in most of these locations, the magnetic field after the transient is different from the field before the transient. These observations are similar to earlier reports (Zhao et al. 2009; Wang et al. 2009; Wang et al. 2011, and references therein) for several M-class and X-class flares.

(iv) The study of the two circular polarization profiles (*LCP* and *RCP*) in the identified kernels indicates that three out of the five locations show a change in line shape (depth and width) at the time of transients in comparison to that of the pre-flare condition. In order to understand the cause of these profile changes, we synthesized the line profiles using the Milne-Eddington atmospheric model. We started with atmospheric parameters that represent pre-flare conditions and showed that a considerable change in DV, magnetic field and source function can lead to the observed changes in *LCP* and *RCP* profiles of the particular kernel at the time of both velocity and magnetic transients. We understand that the simultaneous changes in magnetic and velocity fields are necessary in addition to changes in source functions to cause such changes in the line profiles, particularly close to the points of inflection.

However, it is commonly believed that measurements of the magnetic field are greatly affected by changes in the line profile during the flares. The simulations by Qiu & Gary (2003) suggest that a magnetic reversal is mainly caused by a line changing from absorption to emission and also broadening of the line profile during the flares. Here, in our analysis we reconstructed profiles of Stokes *I* from the *LCP* and *RCP* measurements and we do not find any central reversal or emission at the time of transients (c.f., Fig. 9). Additionally, the line profiles do not show any increase in line width. The location of the kernels in the periphery (c.f., Fig. 2) of the HXR footpoints, with presumably less energy of an impinging particle beam, could be one reason for the absence of central reversal or emission in the observed Stokes *I* profiles. Therefore, we conclude that the changes in the LOS observables seen in the kernels could well be real changes.

In this regard, simultaneous measurements of *LCP* and *RCP* at a better cadence in the future can lead to a better understanding of such transients of velocity and magnetic fields. The best case scenario would be obtaining observations from a slit-based spectrograph with the flaring locations coinciding with the slit.

Acknowledgements This work utilizes data from the Helioseismic and Magnetic Imager (HMI) onboard the *Solar Dynamics Observatory* (*SDO*). This work also utilizes hard X-ray data from *RHESSI*, and Ca II H data from the Solar Optical Telescope (SOT) onboard the *Hinode* mission. Savita Mathur acknowledges support from the NASA grant NNX12AE17G. R. A. García thanks the support of the GOLF CNES grant at the SAp/CEA-Saclay. We are grateful to Dr. S. Couvidat for providing the spectral data from HMI used in our analysis and related discussions. We are thankful to the anonymous referee for useful comments and suggestions that improved the presentation of our manuscript.

References

Couvidat, S., Rajaguru, S. P., Wachter, R., et al. 2012, Sol. Phys., 278, 217
Ding, M. D., Qiu, J., & Wang, H. 2002, ApJ, 576, L83
García, R. A., & Ballot, J. 2008, A&A, 477, 611
Goldreich, P., Murray, N., & Kumar, P. 1994, ApJ, 424, 466
Haber, D. A., Toomre, J., & Hill, F. 1988, in IAU Symposium, 123, Advances in Helio- and Asteroseismology, eds. J. Christensen-Dalsgaard, & S. Frandsen, 59
Hagyard, M. J., Stark, B. A., & Venkatakrishnan, P. 1999, Sol. Phys., 184, 133
Hurford, G. J., Schmahl, E. J., Schwartz, R. A., et al. 2002, Sol. Phys., 210, 61
Kosovichev, A. G. 2011, ApJ, 734, L15
Kosovichev, A. G., & Zharkova, V. V. 1998, Nature, 393, 317
Kosovichev, A. G., & Zharkova, V. V. 1999, Sol. Phys., 190, 459
Kosovichev, A. G., & Zharkova, V. V. 2001, ApJ, 550, L105
Kosugi, T., Matsuzaki, K., Sakao, T., et al. 2007, Sol. Phys., 243, 3
Kumar, B., Mathur, S., García, R. A., & Venkatakrishnan, P. 2010, ApJ, 711, L12
Kumar, B., Venkatakrishnan, P., Mathur, S., Tiwari, S. K., & García, R. A. 2011, ApJ, 743, 29
Leibacher, J. W., & Stein, R. F. 1971, Astrophys. Lett., 7, 191
Leighton, R. B., Noyes, R. W., & Simon, G. W. 1962, ApJ, 135, 474
Lin, R. P., Dennis, B. R., Hurford, G. J., et al. 2002, Sol. Phys., 210, 3
Martínez Oliveros, J. C., Couvidat, S., Schou, J., et al. 2011, Sol. Phys., 269, 269
Maurya, R. A., Vemareddy, P., & Ambastha, A. 2012, ApJ, 747, 134
Metcalf, T. R., Leka, K. D., & Mickey, D. L. 2005, ApJ, 623, L53
Moon, Y.-J., Chae, J., Wang, H., Choe, G. S., & Park, Y. D. 2002, ApJ, 580, 528
Pesnell, W. D., Thompson, B. J., & Chamberlin, P. C. 2012, Sol. Phys., 275, 3
Qiu, J., & Gary, D. E. 2003, ApJ, 599, 615
Ravindra, B., & Howard, T. A. 2010, Bulletin of the Astronomical Society of India, 38, 147
Ravindra, B., Yoshimura, K., & Dasso, S. 2011, ApJ, 743, 33
Schou, J., Borrero, J. M., Norton, A. A., et al. 2012, Sol. Phys., 275, 327
Skumanich, A., & Lites, B. W. 1987, ApJ, 322, 473
Song, Q., Zhang, J., Yang, S.-H., & Liu, Y. 2013, RAA (Research in Astronomy and Astrophysics), 13, 226
Sudol, J. J., & Harvey, J. W. 2005, ApJ, 635, 647
Sun, X., Hoeksema, J. T., Liu, Y., et al. 2012, ApJ, 748, 77
Tiwari, S. K., Venkatakrishnan, P., & Gosain, S. 2010, ApJ, 721, 622
Tsuneta, S., Ichimoto, K., Katsukawa, Y., et al. 2008, Sol. Phys., 249, 167

Vemareddy, P., Ambastha, A., & Maurya, R. A. 2012, ApJ, 761, 60
Wang, H. 2007, in ASPC, 369, New Solar Physics with Solar-B Mission, eds. K. Shibata, S. Nagata, & T. Sakurai, 449
Wang, J., Zhao, M., & Zhou, G. 2009, ApJ, 690, 862
Wang, P., Ding, M.-D., Ji, H.-S., & Wang, H.-M. 2011, RAA (Research in Astronomy and Astrophysics), 11, 692
Wang, S., Liu, C., Liu, R., et al. 2012, ApJ, 745, L17
Wolff, C. L. 1972, ApJ, 176, 833
Zhao, M., Wang, J.-X., Matthews, S., et al. 2009, RAA (Research in Astronomy and Astrophysics), 9, 812
Zharkov, S., Green, L. M., Matthews, S. A., & Zharkova, V. V. 2013, Sol. Phys., 284, 315
Zharkova, V. V., & Zharkov, S. I. 2007, ApJ, 664, 573